ARTICLE   OPEN

Check for updates

Corrosion behavior of an in situ consolidated nanocrystalline Al-V alloy

C. S. Witharamage [1], J. Christudasjustus [1], J. Smith[1], W. Gao[1] and R. K. Gupta [1] ✉

Supersaturated solid solutions of Al and corrosion-resistant alloying elements (M: V, Mo, Cr, Ti, Nb), produced by non-equilibrium processing techniques, have been reported to exhibit high corrosion resistance and strength. The corrosion mechanism for such improved corrosion performance has not been well understood. We present a fundamental understanding of the role of V in corrosion of an Al-V alloy, which will provide a theoretical background for developing corrosion-resistant Al alloys. High-energy ball milling of the elemental powder of Al and V produced an in situ consolidated Al-V alloy, which exhibited high solid solubility of V. The corrosion resistance of Al-V alloy was significantly higher than that of pure Al, which was attributed to the (1) enrichment of V at the passive film/substrate interface, (2) incorporation of V into the passive film, and (3) deposition of V on the iron-containing cathodic particles and therefore, retardation of cathodic reaction.

INTRODUCTION

Global warming and climate change are some of the ongoing severe concerns that the world is facing. The research to reduce fossil fuel consumption via enhancing the fuel efficiency of the vehicles, increasing service life, and reducing material consumption has attracted significant research attention. Therefore, the development of high-strength, lightweight, corrosion-resistant alloys became crucial to meet current technological and environmental challenges. Among most metallic materials in practice, Al alloys exhibit an outstanding strength-to-weight ratio[1]. However, commercially available Al alloys exhibit a tradeoff between mechanical and corrosion properties, limiting their application in many industries. Corrosion and mechanical properties of Al alloys can be controlled by appropriate processing routes along with suitable composition. For example, nanocrystalline Al alloys produced by non-conventional techniques such as sputter deposition[2–4] and ion implantation[5,6] were supersaturated solid solution and exhibited high corrosion resistance.

High-energy ball milling (HEBM), also known as mechanical, alloying is reported to cause amorphization, grain refinements, formation of non-equilibrium phases, and uniform dispersion of immiscible elements, which impart unique properties including simultaneous improvement of corrosion and mechanical properties[7–11]. For instance, Esquivel et al. reported that high-energy ball-milled alloys of Al with corrosion-resistant alloying elements (V) resulted in high strength and corrosion resistance-higher than any commercial alloys[9]. The microstructure of the ball-milled alloys contained fine intermetallics and matrix with high solid solubility of the alloying elements where solid solubility was several orders higher than that predicted by the phase diagrams. The corrosion resistance of the ball-milled Al alloys was high despite a non-uniform microstructure. The improved corrosion resistance of these Al alloys was hypothesized due to one or more of the following mechanisms, which are proposed based on the literature on the sputter-deposited Al alloys, ball-milled alloys Al, and stainless steels[4,12–14].

1. Enrichment of the passive film with the alloying elements improved passivity and decreased passive film breakdown. The proposed mechanism is motivated by the phenomenon causing stainless behavior in Fe–Cr alloys by selective dissolution of Fe and enrichment of Cr in the form of Cr_2O_3.
2. Increased repassivation abilities of the alloys by:

   (a) Prevention of the formation of critical pit solution by lower dissolution rates in the pits and lower hydrolysis of the ions
   (b) Enrichment of the corroding alloy/electrolyte interphase with a corrosion-resistant alloying element
   (c) Redeposition of the solute ions on the cathodic particles (such as Fe containing intermetallics) and decrease the cathodic reaction

3. Release of the oxyanions (i.e., molybdate and vanadate) can inhibit corrosion in initiation stages and accelerate the repassivation.
4. Doping of the passive film with solute ions and therefore increased vacancy annihilation.

Experimental or theoretical verification of the aforementioned mechanisms has not been presented in the literature, mainly because of the unavailability of suitable test specimens and limited resolution of analytical techniques used to study the surface film. The samples produced by the cold compaction of ball-milled powder exhibits significant porosity[15]. Most of the techniques to produce fully consolidated alloys need exposure to high temperatures, which decomposes the supersaturated solid solution to the thermodynamically stable phases[16]. The complex microstructure imposes challenges in developing a mechanistic understanding of corrosion. Therefore, a technique able to produce fully consolidated ball-milled alloys without exposure to high temperatures is desirable to study the ball-milled alloys and their properties.

High-energy ball milling performed under certain specific conditions has been reported to result in fully consolidated samples in the form of coarse particles, discs, or spheres

[1]Department of Materials Science and Engineering, North Carolina State University, Raleigh, NC 27695, USA. ✉email: rkgupta2@ncsu.edu

depending on the material. Such formation of larger particles is termed in situ consolidation (ISC), which has been reported for only a few materials, e.g., Zn[17,18], Cu[19–21], Fe–Cr–Ni[22], Al–Pb–W[23], and Al–Cr[8]. Synthesizing in situ consolidated nanocrystalline Al alloys and studying their properties is beneficial in studying the microstructure and the corrosion mechanisms of ball-milled alloys.

The influences of microstructural features on localized corrosion and the passive film characteristics of high-energy ball-milled Al–V alloys have been investigated herein. The validity of the above-mentioned proposed mechanisms (1–4) has been tested using various electrochemical and characterization techniques. The role of secondary phases in localized corrosion and the influence of the solute on the passive film characteristics, corrosion initiation, and propagation mechanism have been discussed.

RESULTS

Scanning electron microscopic (SEM) and scanning transmission electron microscopic (STEM) analysis

In situ consolidated (ISC) disks of Al-2 at.%V alloy (ISC-Al2V) are shown in Fig. 1a. The diameter of the disks varied from 1 to 5 mm, and thickness was typically 0.5 mm. Backscatter electron (BSE) images and energy-dispersive X-ray spectroscopy (EDXS) analysis showed uniform dispersion of V in Al (Supplementary Fig. 1). Fe-rich particles (Fig. 1b), attributed to the abrasion of milling media during the HEBM process, are confirmed by EDXS analysis (Supplementary Fig. 1). The STEM images of the ISC-Al2V alloy are shown in Fig. 1c, d along with the selected area diffraction (SAD) pattern (Fig. 1e), which reveals a nanocrystalline structure and formation of a supersaturated solid solution of Al-V. The inter planer distance of (111) plane obtained from the SAD pattern was used to determine the lattice parameter (4.042546 Å), which is smaller than that of pure Al (4.04958 Å). Contraction in the lattice can be attributed to the incorporation of V as a solid solution. The solid solubility of the V was estimated to be ~0.89 at.% using the lattice parameters and Vegard's law[24]. The estimated solid solubility of V in Al is ~10^5 times higher than the solubility predicted by the equilibrium phase diagram at room temperature[25]. The high angle annular dark-field (HAADF) images (Fig. 1c, d) revealed the distribution of the V-rich phase and the elongated grains. High magnification HAADF images were used to estimate the grain size (diagonal) and presented in Fig. 1f, which shows a wide variation in the grain size. A small fraction of grains was coarse as 0.5 microns, whereas most grains were <100 nm. STEM analysis revealed homogeneously distributed phases rich in V and appearing bright in Fig. 1c, d.

X-ray diffraction (XRD) analysis

X-ray diffraction scans for the ISC-Al2V alloy and pure Al are shown in Fig. 1g, which showed peaks corresponding to FCC Al and Al$_3$V. Peak broadening and decrease in peak intensity were observed in ISC-Al2V compared to pure Al. A peak corresponding to Al$_3$V intermetallic indicates that HEBM facilitates the formation of both supersaturated solid solution and intermetallic. A peak shift towards a higher 2θ value compared to pure Al was observed in the ISC-Al2V alloy (Supplementary Fig. 2) and was attributed to the reduction of the lattice parameter caused by the formation of the solid solution of V in Al. The solid solubility of V in Al was estimated using XRD analysis (0.92 at.%), consistent with that value estimated from the transmission electron microscopic (TEM) analysis. The average grain size was calculated using peak broadening and was ~45 nm, which is close to the Lorentzian peak of the grain size determined by TEM (Fig. 1f). The formation of a nanocrystalline structure was revealed from both XRD and TEM analysis which agrees with the literature on enhancing grain refinement and formation on non-equilibrium microstructure by HEBM[15,26,27].

Cyclic potentiodynamic polarization (CPP) test

Typical cyclic potentiodynamic polarization curves for ISC-Al2V and pure Al after 30 min of open circuit potential (OCP) stabilization in 0.01 M NaCl are presented in Fig. 2a. The average corrosion potential (E_{corr}), pitting potential (E_{pit}), and corrosion current density (i_{corr}) were derived from the CPP curve fitting and are presented in supplementary Table 1. The average i_{corr} for pure Al in 0.01 M NaCl was 0.12 μA/cm^2, which is ~2 times higher than that in ISC-Al2V alloy. The E_{pit} of ISC-Al2V was 479 mV$_{SCE}$ higher than that in pure Al (99.99% purity). The higher corrosion resistance of ISC-Al2V alloy, as evident from higher E_{pit} and lower i_{corr} could be attributed to the uniform dispersion of V in Al, extended solid solution of V in Al, and nanocrystalline structure[8,10,11].

The formation of critical pit solution (CPS) due to the hydrolysis of the cations within the pit and migration of Cl$^-$ from the electrolyte is necessary for the pit growth, and any conditions ceasing the CPS formation would cause repassivation. The addition of V in ISC-Al2V may decrease the dissolution of the alloy to the level that a critical pit solution is not formed[2]. The addition of V may also increase the stability of the passive film at lower pH, which could cause repassivation inside the pits[13]. To comprehend this phenomenon about the influence of V, CPP was performed in 0.1 M HCl (Supplementary Fig. 3), which showed considerably lower corrosion current density and anodic current density in ISC-Al2V, confirming obstacles in the formation of CPS.

Electrochemical impedance spectroscopy (EIS) analysis

Electrochemical impedance spectroscopy measures the passive film resistance and ionic transportation through the passive film. EIS measurements were performed for 14 days at regular time intervals. The Nyquist plots for both ISC-Al2V and pure Al are shown in Fig. 2b. Both ISC-Al2V and pure Al are characterized by two-time constants, one at high frequencies and the second at low frequencies. These two-time constants correspond to the passive film and localized corrosion, respectively[28,29]. The experimental data fitting was carried out using Zview software and the equivalent circuit shown in Fig. 2c, where, R_S is the solution resistance, CPE_{film} and R_{film} represent the film constant phase element and the resistance of the film, respectively, CPE_{dl} and R_{ct} denote the double layer constant phase element and charge transfer resistance, respectively. A constant phase element represents a deviation from an ideal capacitor.

Both ISC-Al2V and pure Al revealed a continuous increment of the total impedance (|Z|) over the immersion time (Fig. 2b). The R_{film} and R_{ct} of ISC-Al2V after 12 h of immersion were much higher than that in pure Al, indicating higher corrosion resistance in ISC-Al2V than that in pure Al. Both ISC-Al2V and pure Al showed R_{film} increment over the immersion time (Supplementary Table 2). R_{film} for pure Al and ISC-Al2V was almost similar after 336 h of immersion. Nevertheless, ISC-Al2V displayed a significant increment of R_{ct} over the immersion time until 336 h. The improved R_{ct} in ISC-Al2V could be attributed to the formation of corrosion products inside the pit that can partially block the formed pits, which could act as a barrier for ion transportation between electrolyte and substrate[30], whereas the R_{ct} after 12 h of immersion of pure Al dropped noticeably after 48 h and increased gradually over the immersion time until 336 h. The CPE_{film} and CPE_{dl} were noticeably lower for ISC-Al2V compared to that in pure Al. In ISC-Al2V, the CPE_{film} was increased until 96 h and gradually declined with the continuous immersion, probably due to the passive film growth rather than the influence of hydration. The CPE_{dl} for ISC-Al2V dropped from 12 to 96 h followed by gradual increment, whereas in pure Al, CPE_{film} and CPE_{dl} increased over the immersion time. The corrosion resistance improvement of ISC-Al2V in the long-term EIS tests is attributed to the enhancement of
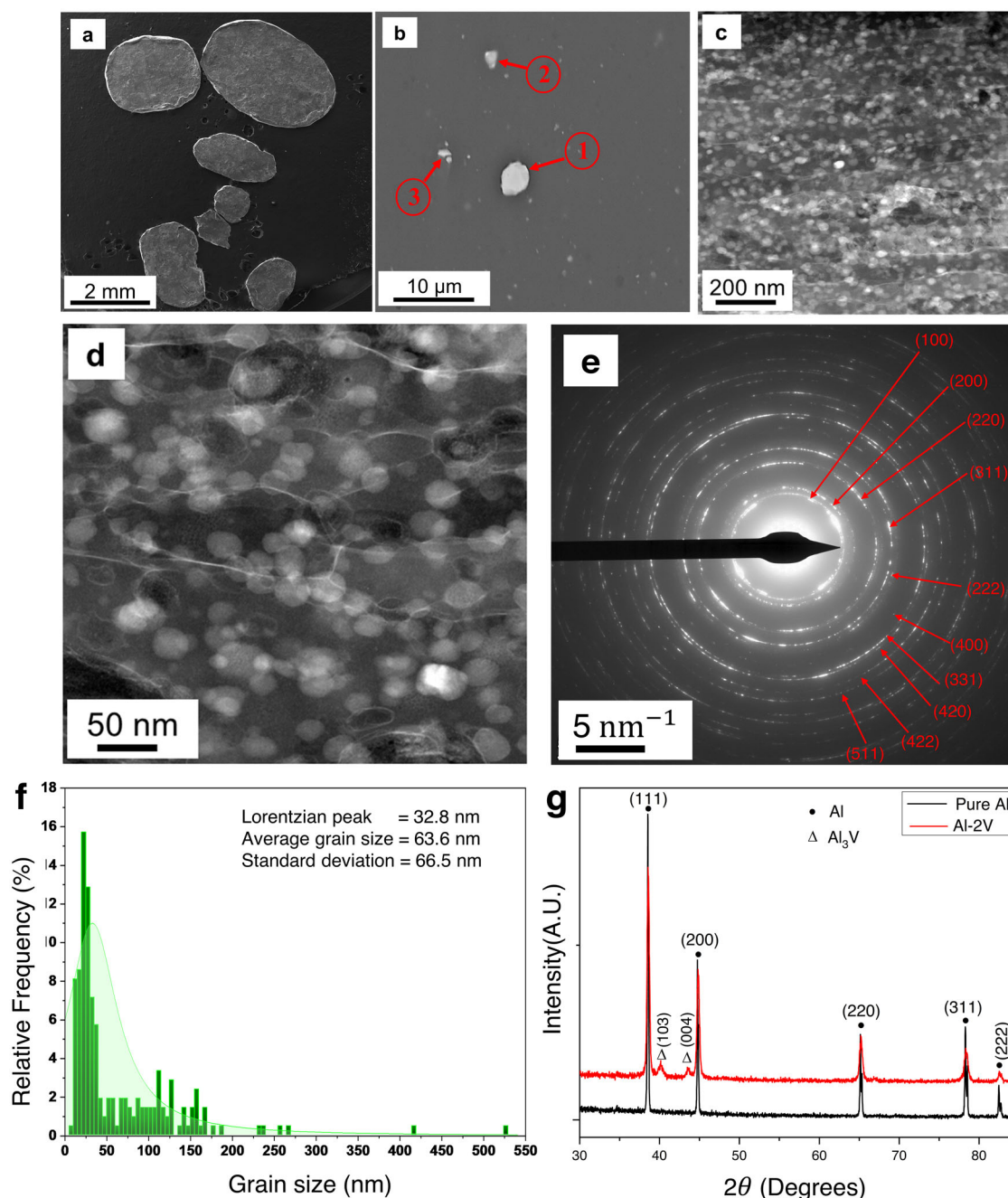
Fig. 1 Microstructural characterization of ISC-Al2V alloy. a BSE image of the whole samples, **b** zoomed-in region showing the Fe rich particles marked by the arrows, **c** HAADF STEM revealing the distribution of V-rich phase, **d** HAADF image illustrating the grain size, **e** SAD pattern, **f** grain size distribution estimated from the SAD pattern shown in (**e**), **g** XRD scans of ISC-Al2V alloy comparison with pure aluminum.

both R_{film} and R_{ct} compared to that in pure Al. However, R_{ct} enhancement in the alloy is significantly higher that R_{film} increment, which could be suggested to the enhancement of the pitting corrosion resistance with an increase in the immersion time. An increase in pitting corrosion resistance could occur because of (1) change in the surface of the alloy within the pits, i.e., enrichment of the V near electrolyte/alloy interface within the pit, (2) repassivation due to decreased cathodic activities of cathodic sites (initiation sites for pitting), (3) inability to form CPS and therefore repassivation. These factors are discussed in the following sections.

Defect concentration in the passive film using Mott–Schottky analysis

Mott–Schottky analysis of ISC-Al2V and pure Al after immersion in 0.01 M NaCl for 30 min was performed (Fig. 2d) to evaluate the passive film and understand the presence of point defects. A positive slope was noticed in both ISC-Al2V, and pure Al, which revealed that the formed passive films are n-type semiconductors. It has been widely accepted that the donors such as oxygen vacancies and cation interstitials are the dominant charge carriers in n-type passive films[31,32]. The average donor density of ISC-Al2V was $\sim(1.906 \pm 0.32) \times 10^{18} \, \text{cm}^{-3}$ which is ~1.66 times lower than
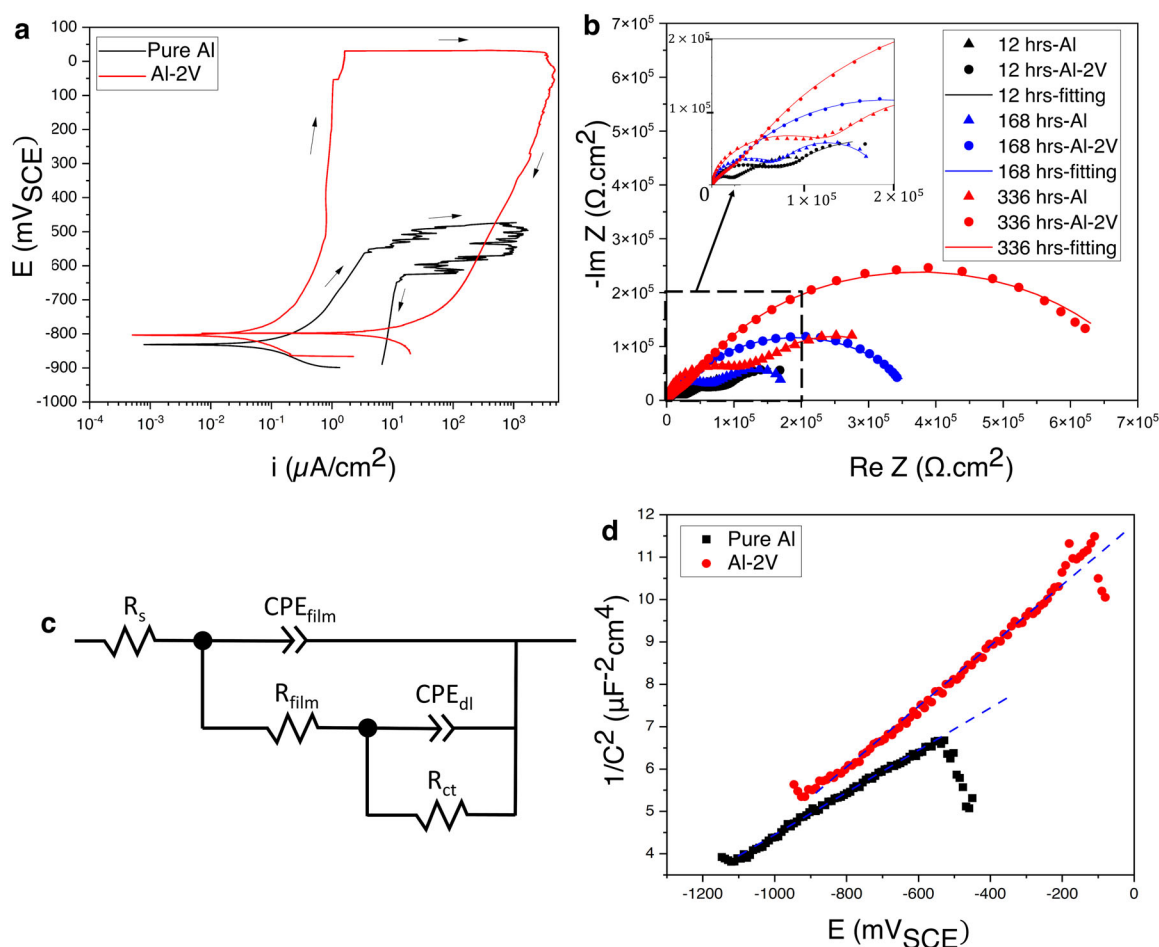
Fig. 2 Electrochemical behavior of ISC-Al2V alloy in comparison with pure Al in 0.01 M NaCl. a Representative CPP curves after 30 min of OCP stabilization, **b** Nyquist curves at OCP for various immersion times, **c** the equivalent circuit diagram used for EIS data fitting for both ISC-Al2V and pure Al, **d** Mott–Schottky curves with trend lines (blue dotted) after 30 min of stabilization.

that in pure Al. A lower density signifies higher corrosion resistance.

X-ray photoelectron spectroscopy (XPS) and secondary ions mass spectrometry (SIMS)

The X-ray photoelectron spectroscopy and time-of-flight secondary ions mass spectrometry analysis were performed on ISC-Al2V after polishing and immersion in 0.1 M NaCl solution for 0 min, 5 min, 30 min, and 2 days. XPS survey scans detected Al, O, and V. Supplementary Fig. 4 shows the survey scans, and the elemental distribution is presented in supplementary Table 3. High-resolution regional scans of O, Al, and V are presented in Fig. 3. The O 1s peak was deconvoluted into two peaks named as O $1S_A$ and O $1S_B$. The O $1S_A$ peak at lower binding energy (~532.5 eV) was attributed to the oxide contribution, and the O $1S_B$ peak at higher binding energy (~533.7 eV) was associated with the hydroxide and/or oxygen bonded carbon contamination. Figure 3b represents Al 2p peak with two binding energies: A peak with lower binding energy at ~72.9 eV corresponded to metallic Al and the higher binding energy (~75.6 eV) associated with Al oxide/hydroxide peak[33]. Each Al peak was further deconvoluted into two peaks: The metallic Al peak deconvoluted into $2p_{3/2}$ (~72.8 eV) and $2p_{1/2}$ (~73.2 eV). An Al_2O_3 peak at ~75.3 eV and $Al(OH)_3$ peak at ~75.9 eV were obtained from the deconvolution of the oxide/hydroxide peak. The intensity of the Al oxide/hydroxide peak increased with the immersion time, whereas the intensity of the metallic peak decreased over the immersion time; it could be

attributed to the film growth on the surface. Due to a thick surface layer, the metallic Al peak was not detected after 2 days of immersion. The film thickness, calculated using the method reported in the literature[34,35], was 2.97, 3.02, and 4.95 nm for 0, 5, and 30 min of immersion time, respectively. The O/Al atomic ratio was estimated from O 1s and Al 2p air-formed peaks (Supplementary Table 3). The estimated O/Al atomic ratio was 2.43, more significant than the stoichiometric value of 1.5 (i.e., Al_2O_3), attributed to hydroxide formation. The O/Al ratio was increased over the immersion time and reached 3.10, which is closer to the O/Al ratio in $Al(OH)_3$. The continuous hydration of the oxide layer and formation of an external $Al(OH)_3$ could be attributed to the increase in the O/Al ratio with immersion time. Moreover, oxides or hydroxides of V also contribute to the overall oxygen content of the passive film. Figure 3c shows the experimental V 2p peak and the four deconvoluted peaks representing four different oxidation states of V (i.e., V^{0+}, V^{3+}, V^{4+}, and V^{5+}). The intensity of the metallic V peak was highest in air-formed and gradually decreased over the immersion time. The V^{4+} content was the highest among all the oxidized V in all the four immersion conditions, followed by V^{3+} and then V^{5+}. A gradual decrease in V^{5+} content was noticed over the immersion time.

The secondary ion mass spectrometry (SIMS) analysis for ISC-Al2V shows depth profiles for $^{18}O^-$, OH^-, Al_2^-, AlO_2^-, VO^-, and V^-. The ions Al_2^- (53.9636 amu) and AlO_2^- (58.9719 amu) corresponds to metallic Al and Al oxide, respectively[36,37]. The oxygen characteristic for the oxide scale is presented by the $^{18}O^-$ (17.9997 amu) since the $^{16}O^-$ (15.9955 amu) saturates the
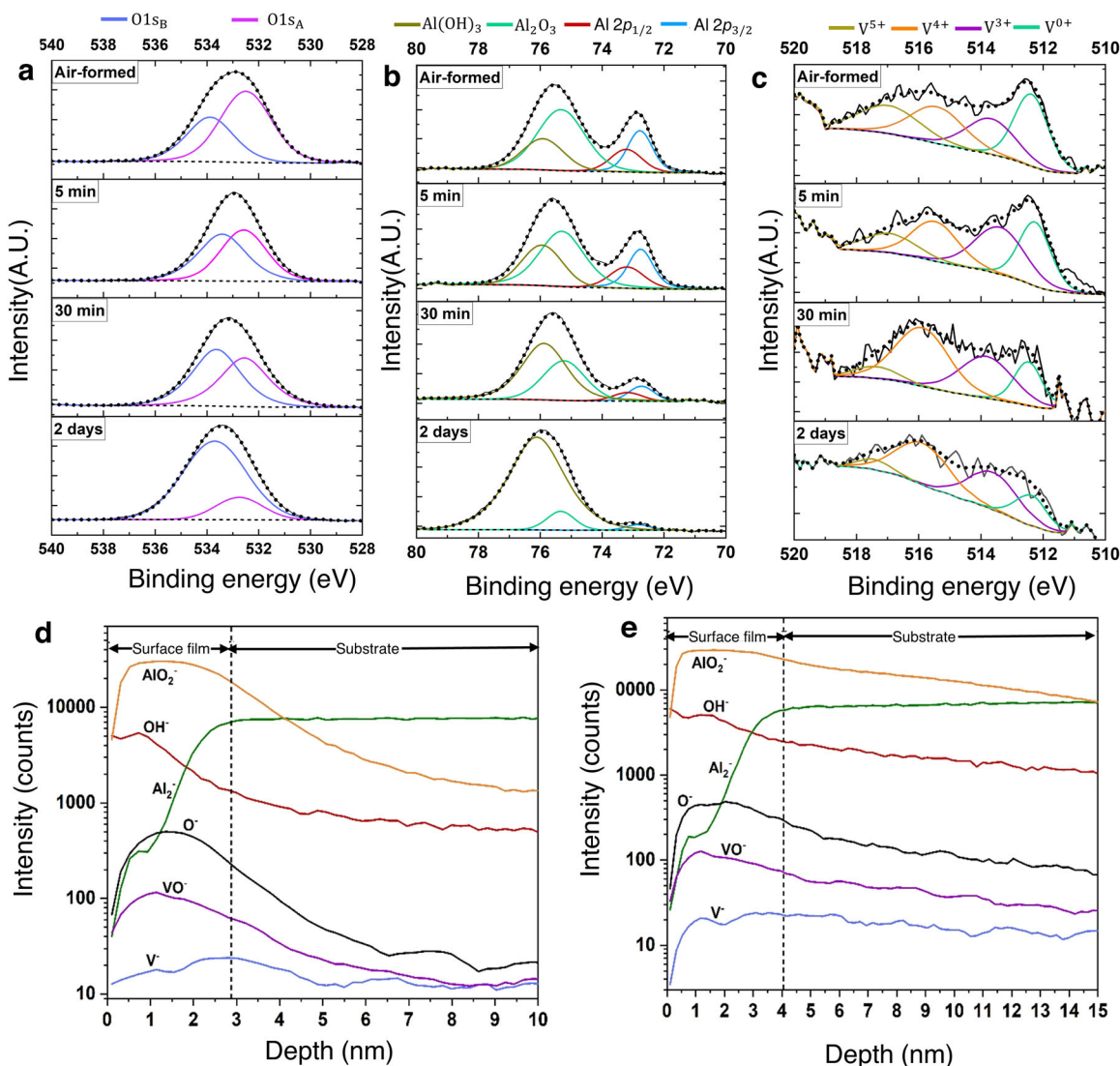
Fig. 3 Surface film characterization of ISC-Al2V. a–c XPS regional scan of O 1s, Al 2p, and V 2p$_{3/2}$ peaks following immersion in 0.1 M NaCl for various times. The spectra are shown in thin solid lines, envelope in dotted lines, and background in dashed lines. **d, e** ToF-SIMS negative ion depth profiles of ISC-Al2V for air-formed and 30 min of immersion in 0.1 M NaCl solution, respectively.

detector. The metallic and oxidized V is shown by V$^-$ (50.9445 amu) and VO$^-$ (66.9394 amu). Two regions were defined as surface film and the metallic substrate, separated by the dotted lines (Fig. 3d, e). Moreover, the metallic substrate begins once the Al$_2^-$ curve reaches the plateau. The surface film thickness was ~2.88, 3.10, 4.06, and 35.63 nm for 0 min, 5 min, 30 min, and 2 days of immersion. ^{18}O$^-$, OH$^-$, AlO$_2^-$, V$^-$, and VO$^-$ were observed in the surface film in all four conditions exhibit the presence of both metallic and oxidized V in the passive film. A slight increment of V$^-$ ions was observed at the substrate/surface film interface in both air-formed and 5 min (Supplementary Fig. 5a); immersed samples exhibit the enrichment of metallic V at the substrate/ surface film. This metallic V enrichment at the substrate/surface film interface may be a barrier to the further dissolution/oxidation of the aluminum[13]. After 2 days of immersion, the V enriched layer was shifted towards the surface film/electrolyte interface (Supplementary Fig. 5b). The VO$^-$ ion enrichment was observed near the middle of the surface film in all four conditions. This incorporation of V in the passive film and development of V enriched layer is expected to contribute to observed enhancement in corrosion resistance.

Characterization of the passive film and pits using STEM

STEM cross-section images of the passive film and pit for ISC-Al2V alloy after 30 min of immersion in 0.1 M NaCl are shown in Figs. 4 and 5. Figure 4a shows the formation of a uniform passive film with an average thickness of 5.6 nm, consistent with the passive film thickness estimated from XPS and SIMS. The EDXS elemental mapping was performed on the region in Fig. 4b (HAADF), revealing Al, O, and V (Fig. 4c–f). The O was distributed on the top of the alloy surface, confirming a uniform passive film (Fig. 4e). Figure 4f shows the enrichment of V underneath the passive film, which agrees with the enrichment of V observed at the surface film/substrate interface through SIMS analysis. The V content was estimated using an EDXS line scan along with the red arrow (Fig. 4f). The highest V content was observed underneath the passive film (Fig. 4g).

A cross-sectional image of a pit developed after immersion in 0.1 M NaCl for 30 min is presented in Fig. 5a. The pit growth was insignificant even after 2 days of immersion (Supplementary Fig. 6). The EDXS analysis was performed on the magnified cross-sectional image of the pit (Fig. 5b–f), confirming the presence of Fe-rich particles inside the pit. Fe containing intermetallics are cathodic and initiate corrosion in Al[38]. V was observed on the Fe-
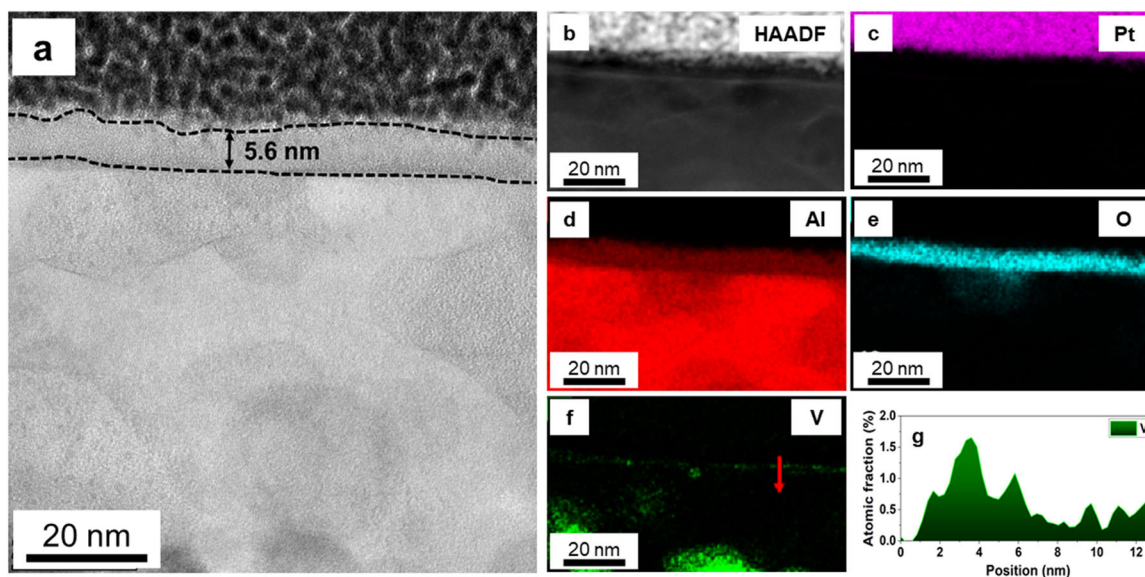
Fig. 4 Structure of the passive film of ISC-Al2V alloy. a STEM image showing the uniform passive film, **b** zoomed-in HAADF STEM image, **c–f** EDXS elemental mapping of the same region in (**b**) and, **g** distribution of V along the red arrow in (**f**) revealing the V enrichment at the oxide/metal interface.

rich particles (Fig. 5f), indicating the V deposition during corrosion inside the pit and, therefore, decreased cathodic activity of Fe-rich pitting and repassivation in the early stages of pitting corrosion. The corrosion inhibition mechanism of V could be analogs corrosion inhibition of vanadate corrosion inhibitor[39,40]. In addition, enrichment of V under the corrosion product layer and within the corrosion products in the pit is observed (Fig. 5f). The net intensity of V was estimated along with the red arrow indicated in Fig. 5f. The V content underneath the pit was slightly higher than that in the matrix region (Fig. 5g), revealing V enrichment underneath the pit. The observed phenomenon of V deposition on the Fe-rich particles and incorporation of V in corrosion produced within the pits is confirmed by the TEM study of ISC-Al2V alloy after 2 days of immersion (Supplementary Fig. 6). The size of the pits after 30 min and 2 days of immersion was almost similar, indicating inhibition of the corrosion in the early stages of initiation.

DISCUSSION
Both XPS and SIMS revealed the incorporation of metallic and oxidized V into the passive film developed on ISC-Al2V. This oxidized V species (i.e., V^{n+} ($n = 3,4,5$)) in the passive film of ISC-Al2V could interact with oxygen vacancies. Therefore, the number of oxygen vacancies decreased compared to the pure Al, as observed in the Mott–Schottky analysis (Fig. 2d). The doping of solute V with oxygen vacancies present in the passive film could be attributed to the formation of complex species that have neutral and null mobility. Chloride was not detected by the SIMS and XPS. It should be noted that the incorporation of Cl to the passive film is attributed to the localized corrosion of Al[41,42]. The absence of chloride shows the effectiveness of V in preventing Cl incorporation to the passive film and therefore improving pitting corrosion resistance.

The enrichment of the V-rich layer underneath the passive film was observed by both TEM and SIMS. Moreover, Supplementary Fig. 7 revealed that V-rich phase became a part of the passive film instead of the dissolution during passive film formation. The observed enrichment of V underneath passive film is attributed to higher dissolution kinetics of Al than V. The incorporation of both metallic and oxidized V in the passive film and the enrichment of

V underneath the film enhances the passive film stability. Consequently, the passive film resistance (EIS analysis), pitting potential, and the passive window (in the CPP curve) increase in ISC-Al2V compared to pure Al.

The schematic representation of pit initiation and repassivation in the early stages of pitting corrosion is shown schematically in Fig. 6. The pitting corrosion in ISC-Al2V initiates at the interface of Fe-rich particles and matrix. Fe-rich particles are reported to be cathodic in nature[38], i.e., act as a site for the cathodic reaction (i.e., oxygen reduction reaction), and introduce an alkaline environment around them and localized dissolution of the passive film[43]. Subsequently, the interaction between the alloy substrate and the electrolyte caused the rapid oxidation of Al that led to the pit initiation (Fig. 6a). The hydrolysis of the metal cations causes localized acidification within the pit, and chloride ion transportation occurs toward the pit to maintain the charge neutrality inside the pit[44]. The enriched V layer underneath the pit (Fig. 6b) has two effects (1) low dissolution rate (Supplementary Fig. 3) and therefore inability to sustain a critical pit solution necessary for pit growth and (2) release of oxidized vanadium species (vanadates), which are well-known corrosion inhibitors[39,40]. The disposition of V (Figs. 5 and 6b) on Fe-rich particles is attributed to the decrement in the cathodic efficiency of the Fe-rich particles and eventually repassivation of the pit at very early stages of corrosion. The deposition of V on Fe-rich particles is a significant finding and indicates that uniform dispersion of the alloying elements that can form corrosion inhibitors could potentially cause repassivation at the early stage of corrosion.

In summary, ISC-Al2V alloy exhibited enhancement of corrosion resistance, significantly higher than pure Al. A combination of electrochemical and analytical techniques provided an understanding of the corrosion mechanisms. The improved corrosion resistance of ISC-Al2V alloy is attributed to inhibition of pitting corrosion by the disposition V on the cathodic iron-containing particle, the enhancement of passive film stability due to the incorporation of V species in the passive film, and the enrichment of V at the passive film/substrate interface. Mechanisms for the improved corrosion resistance presented herein are expected to facilitate the determination of corrosion-resistant microstructures, selection of alloying elements, choice of manufacturing
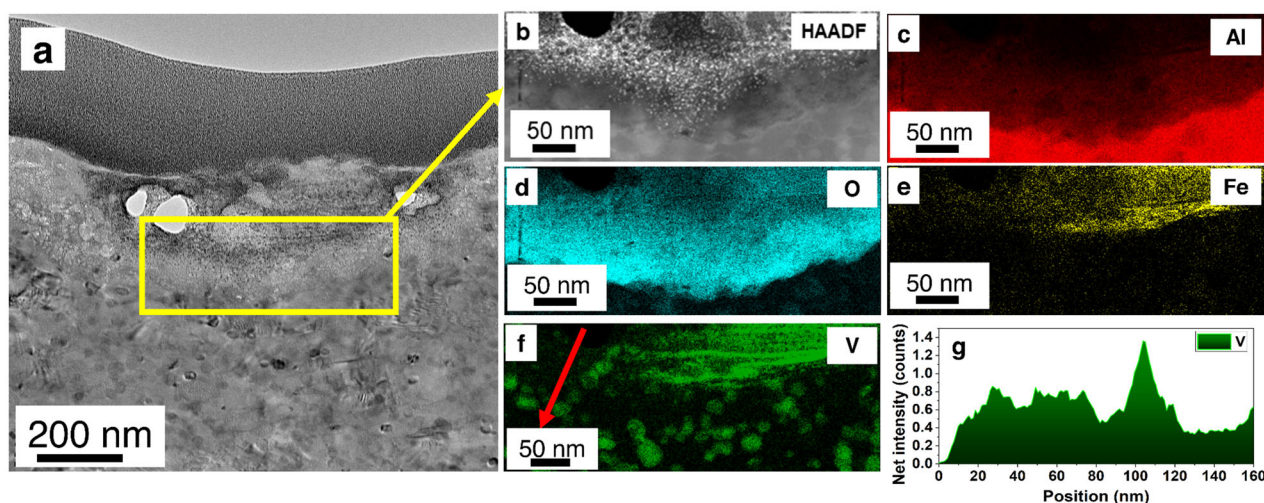
Fig. 5 Pit morphology of ISC-Al2V alloy. a STEM cross-section sample prepared by FIB revealing the pit morphology after 30 min of immersion in 0.1 M NaCl, **b** zoomed-in HAADF image, **c–f** EDXS elemental mapping of the region in (**b**), and **g** distribution of V along the red arrow in (**f**) revealing the V enrichment underneath pit.
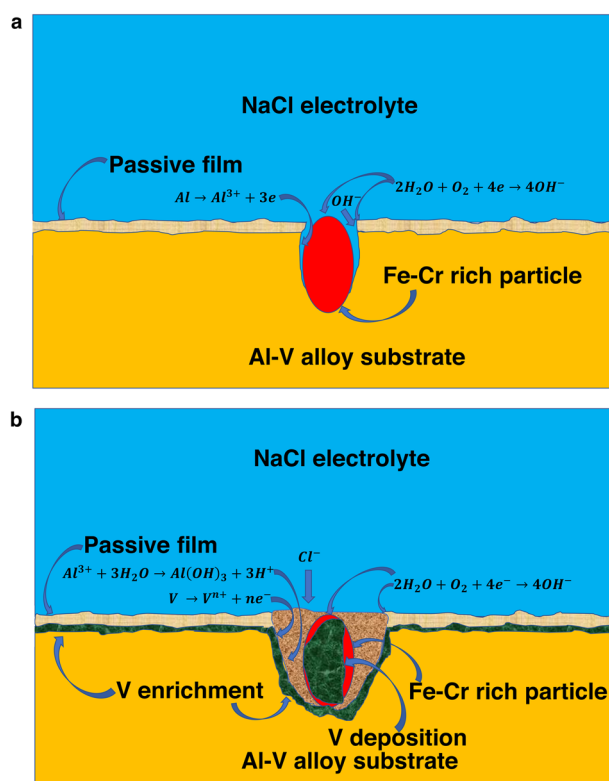

Fig. 6 Schematic representation of the proposed corrosion and inhibition mechanisms. a Localized corrosion initiation around the Fe–Cr rich particle and **b** corrosion inhibition due to the deposition of V on Fe–Cr particle and enrichment of V under the passive film.

technologies for desired microstructure, and therefore facilitate the development of high strength and corrosion-resistant Al alloys.

METHODS

Alloy synthesis

ISC-Al2V alloy was produced using the Fritsch P-5/4 planetary ball mill. aluminum powder (purity 99.7% with 0.09% of iron, and 0.03% of silicon and mesh size − 50/+100) and vanadium powder (purity 99.8% and mesh size 325) were weighted inside the glove box with a high purity argon environment (oxygen <25 ppm). The steel balls with 10 mm diameter were loaded into the jar. The ball-to-powder weight ratio was kept at 16:1. The weighted alloy powders (aluminum and vanadium) with the process controlling agent (1.5 wt% Stearic acid) were filled into the jar and sealed inside the glove box. High-energy ball milling was performed at 350 RPM for 100 h. The milling was paused for 30 min after each 1 h of milling to avoid overheating.

Characterization

Scanning electron microscopy and energy-dispersive X-ray spectroscopy. The SEM was performed using a field emission scanning microscope FEI Verios 460 L at 20 kV accelerating voltage. The sample was grounded up to 1200 grit using SiC papers. The fine polishing up to 0.05 μm was carried out using colloidal silica suspension followed by ultrasonication in ethanol for 10 min BSE images and EDXS elemental mapping for Al, V, Fe, and O were performed on the sample to understand the microstructure and the elemental distribution.

Scanning transmission electron microscopy

The electron microscopy and spectroscopic analysis were conducted using a Thermo Scientific Titan aberration-corrected STEM operated at 200 kV. HAADF and bright-field (BF) images were obtained for ISC-Al2V alloy samples after 30 min and 2 days of immersion in 0.1 M NaCl. The samples were polished up to 0.05 μm, followed by ultrasonic cleaning. The focused ion beam (FIB) technique was used to prepare the cross-sectional TEM samples. An e-beam deposition of 300 nm Pt layer on the selected region followed by an ion beam deposition of 200 nm Pt layer on top was used to protect the surface during FIB. The EDXS elemental mapping was carried out to analyze the Al, V, O, Pt, and Fe distribution in each sample.

X-ray diffraction

XRD was performed using the Rigaku SmartLab X-ray diffractometer with a Cu Kα radiation (λ = 0.15406 nm) filter. The XRD pattern was recorded in the 2θ range from 30 to 85° with a step size of 0.02° and a scanning rate 1° per min. The average grain size was calculated using Scherrer's formula[45,46] after subtracting instrumental broadening. The reported literature referred to the calculation of grain size and solid solubility[9,15,24,46].

X-ray photoelectron spectroscopy

The passive film chemical composition of ISC-Al2V was studied in 0 min, 5 min, 30 min, and 2 days of immersion in 0.1 M NaCl solution using SPECS XPS. The loose contamination was removed from the sample surface using DI water after the immersion test. The total vacuum

chamber pressure was maintained below 10^{-9} mbar, and Mg anode was used as the X-ray source of 300 W. The experiment was performed on the scan area of 2×2 mm with a take-off angle of 60°. The survey scan was obtained from 0 to 1100 eV binding energy to obtain the elements present on the surface. At the same time, high-resolution spectra were performed to identify the present elements in the passive film and their oxidation states. The binding energies were calibrated with the peak of C1s at 285.0 eV. High-resolution spectra of 1s peak for C and O, 2p peak for Al and V were recorded. The spectrum analysis was conducted using CASA software, considering background subtraction and relative sensitivity factors given by Scofield[33].

Secondary ions mass spectroscopy

Elemental depth profiling was carried out for ISC-Al2V in 0 min, 5 min, 30 min, and 2 days immersion in 0.1 M NaCl solution using the time-of-flight secondary ion mass spectroscopy (ToF-SIMS). The chamber pressure was maintained below 5×10^{-9} mbar in high mass resolution mode, and sputtering was performed using a Cs+ ion beam with 1 keV and 7.2 nA target current over a 100×100 µm raster area. The target current was restored over an area of 20×20 µm using a Bi3+ primary ion source with 25 keV and 0.32 pA. The negative ion profiles were recorded due to the higher sensitivity to fragments from the oxide region. The depth scale was calibrated using surface profilometry with the air-formed sample.

Electrochemical measurements

The specimens for corrosion testing were mounted in epoxy and grounded to 1200 grit SiC paper finish followed by ultrasonication in ethanol for 10 min. The sample edges were sealed by epoxy resin (Araldite) and stored in a desiccator for about 12 h before testing (This method avoided crevice corrosion during the electrochemical test). A conventional three-electrode flat cell with the Pt mech counter electrode and saturated calomel reference electrode (SCE) was utilized for the experiment. Potentiodynamic polarization, EIS, and Mott–Schottky tests were performed using VMP-300 potentiostat (Biologic) with the help of the EC-lab software. All the electrochemical tests were repeated at least three times to ensure reproducibility.

Potentiodynamic polarization

ISC-Al2V and pure Al samples were immersed for 30 min in a 0.01 M NaCl for stabilization. The anodic polarization was performed separately with the sweep rate of 0.167 mV/s starting from 50 mV$_{SCE}$ below the (OCP) toward the more positive potential direction. The scanning direction was reversed once the current reached 200 µA/cm^2. The same procedure was followed with 0.1 M HCl instead of 0.01 M NaCl to understand the passive film stability at low pH conditions.

Electrochemical impedance spectroscopy

EIS measurements for the ISC-Al2V and pure Al were carried in a 0.01 M NaCl solution using the AC sinusoidal voltage signal with 10 mV amplitude and frequency range of 100 kHz to 1 mHz. The EIS tests were performed over 14 days. The data was collected after every 12 h.

Mott–Schottky analysis

The Mott–Schottky analysis was performed for both ISC-Al2V and pure Al. The sinusoidal voltage signal with 10 mV amplitude and 1 kHz frequency was used for both samples. The Mott–Schottky analysis was carried after 30 min of immersion in 0.01 M NaCl. The scanning was done with 80 potential steps starting from 50 mV$_{SCE}$ below OCP towards the more noble direction. At least three tests of measurements were carried out to ensure reproducibility.

DATA AVAILABILITY

The data that support the findings in this study is available upon a reasonable request.

REFERENCES

1. Dorward, R. C. & Pritchett, T. R. Advanced aluminium alloys for aircraft and aerospace applications. *Mater. Des.* **9**, 63–69 (1988).
2. Frankel, G. S., Newman, R. C., Jahnes, C. V. & Russak, M. A. On the pitting resistance of sputter-deposited aluminum alloys. *J. Electrochem. Soc.* **140**, 2192–2197 (1993).
3. Davis, G. D., Moshier, W. C., Fritz, T. L. & Cote, G. O. Evolution of the chemistry of passive films of sputter-deposited, supersaturated Al alloys. *J. Electrochem. Soc.* **137**, 422–427 (1990).
4. Metikoš-Hukovi, M., Radi, N., Grubač, Z. & Tonejcv, H. A. The corrosion behavior of sputter-deposited aluminum-tungsten alloys. *Electrochim. Acta* **47**, 2387–2397 (2002).
5. Natishan, P. M., McCafferty, E. & Hubler, G. K. Localized corrosion behavior of aluminum surface alloys produced by ion implantation and ion beam mixing. *Mater. Sci. Eng. A* **116**, 41–46 (1989).
6. Natishan, P. M., McCafferty, E. & Hubler, G. K. The corrosion behavior of Mo-Al, Cr-Al and Cr-Mo-Al surface alloys produced by ion beam mixing and ion implantation. *Corros. Sci.* **32**, 721–731 (1991).
7. Gupta, R. K., Fabijanic, D. & Dorin, T. Simultaneous improvement in the strength and corrosion resistance of Al via high-energy ball milling and Cr alloying. *Mater. Des.* **84**, 270–276 (2015).
8. Gupta, R. K., Fabijanic, D., Zhang, R. & Birbilis, N. Corrosion behaviour and hardness of in situ consolidated nanostructured Al and Al-Cr alloys produced via high-energy ball milling. *Corros. Sci.* **98**, 643–650 (2015).
9. Esquivel, J., Murdoch, H. A. & Darling, K. A. Excellent corrosion resistance and hardness in Al alloys by extended solid solubility and nanocrystalline structure. *Mater. Res. Lett.* **6**, 79–83 (2018).
10. Esteves, L. et al. Effect of V content on corrosion behavior of high-energy ball milled AA5083. *Corros. Sci.* **186**, 109–465 (2021).
11. Esteves, L. et al. Corrosion behavior of AA5083 produced by high-energy ball milling. *J. Alloy. Compd.* **857**, 158–268 (2021).
12. Esquivel, J. & Gupta, R. K. Review—Corrosion-resistant metastable Al alloys: an overview of corrosion mechanisms. *J. Electrochem. Soc.* **167**, 081504 (2020).
13. Davis, G. D., Shaw, B. A., Rees, B. J. & Ferry, M. Mechanisms of passivity of nonequilibrium Al-W alloys. *J. Electrochem. Soc.* **140**, 951–959 (1993).
14. Davis, G. D., Shaw, B. A., Rees, B. J. & Pecile, C. A. Electrochemical behavior and surface chemistry of non-equilibrium aluminum–tantalum alloys: solute-rich interphase mechanisms. *Surf. Interface Anal.* **23**, 609–617 (1995).
15. Esquivel, J. & Gupta, R. K. Influence of the V content on microstructure and hardness of high-energy ball milled nanocrystalline Al-V alloys. *J. Alloy. Compd.* **760**, 63–70 (2018).
16. Xu, J., Collins, G. S., Peng, L. S. J. & Atzmon, M. Deformation-assisted decomposition of unstable Fe$_{50}$Cu$_{50}$ solid solution during low-energy ball milling. *Acta Mater.* **47**, 1241–1253 (1999).
17. Zhang, X., Wang, H., Scattergood, R. O., Narayan, J. & Koch, C. C. Evolution of microstructure and mechanical properties of in situ consolidated bulk ultra-fine-grained and nanocrystalline Zn prepared by ball milling. *Mater. Sci. Eng. A* **344**, 175–181 (2003).
18. Zhang, X., Wang, H. & Kassem, M. Preparation of bulk ultrafine-grained and nanostructured Zn, Al and their alloys by in situ consolidation of powders during mechanical attrition. *Scr. Mater.* **46**, 661–665 (2002).
19. Sikdar, K., Chakravarty, S. & Roy, D. Synthesis and characterization of an in situ consolidated nanocrystalline Cu$_{88}$Al$_{11.5}$Y$_{0.5}$ alloy. *J. Alloy. Compd.* **717**, 219–225 (2017).
20. Cheng, S., Ma, E., Wang, Y. M. & Kecskes, L. J. Tensile properties of in situ consolidated nanocrystalline Cu. *Acta Mater.* **53**, 1521–1533 (2005).
21. Youssef, K. M., Abaza, M. A. & Scattergood High strength, ductility, and electrical conductivity of in-situ consolidated nanocrystalline Cu-1%Nb. *Mater. Sci. Eng. A* **711**, 350–355 (2018).
22. Gupta, R. K., Darling, K. S. & Singh Raman, R. K. Synthesis, characterization and mechanical behaviour of an in situ consolidated nanocrystalline FeCrNi alloy. *J. Mater. Sci.* **47**, 1562–1566 (2012).
23. Varam, S., Prasad, M. D., Rao, K. B. S. & Rajulapati, K. V. Mechanical properties of in situ consolidated nanocrystalline multi-phase Al–Pb–W alloy studied by nanoindentation. *Philos. Mag.* **96**, 3671–3685 (2016).
24. Uesugi, T. & Higashi, K. First-principles studies on lattice constants and local lattice distortions in solid solution aluminum alloys. *Comput. Mater. Sci.* **67**, 1–10 (2013).
25. Esquivel, J., Wachowiak, M. G., O'Brien, S. P. & Gupta, R. K. Thermal stability of nanocrystalline Al-5at.%Ni and Al-5at.%V alloys produced by high-energy ball milling. *J. Alloy. Compd.* **744**, 651–657 (2018).
26. Witharamage, C. S., Christudasjustus, J. & Gupta, R. K. The effect of milling time and speed on solid solubility, grain size, and hardness of Al-V alloys. *J. Mater. Eng. Perform.* **30**, 3144–3158 (2021).

27. Witharamage, C. *The Influence of Ball Milling Time on Solid Solubility, Grain Size and Hardness of Al-V Alloys.* MS Thesis, The University of Akron (OhioLINK Electronic Theses and Dissertations Center, 2020).

28. Meng, Y. et al. Pitting of 2024 alloys prepared by spark plasma sintering using powders with different sizes. *Corros. Sci.* **170**, 108525 (2020).

29. Huo, W. et al. Simultaneously enhanced mechanical strength and inter-granular corrosion resistance in high strength 7075 Al alloy. *J. Alloy. Compd.* **781**, 680–688 (2019).

30. Moreto, J. A., Marino, C. E. B., Bose Filho, W. W., Rocha, L. A. & Fernandes, J. C. S. SVET, SKP and EIS study of the corrosion behaviour of high strength Al and Al-Li alloys used in aircraft fabrication. *Corros. Sci.* **84**, 30–41 (2014).

31. Fattah-alhosseini, A. & Sabaghi Joni, M. Semiconducting behavior of the anodically passive films formed on AZ31B alloy. *J. Magnes. Alloy.* **2**, 305–308 (2014).

32. Liu, J. & Macdonald, D. D. The passivity of iron in the presence of ethylenediaminetetraacetic acid. II. The defect and electronic structures of the barrier layer. *J. Electrochem. Soc.* **148**, B425 (2001).

33. Scofield, J. H. Hartree-Slater subshell photoionization cross-sections at 1254 and 1487 eV. *J. Electron Spectros. Relat. Phenom.* **8**, 129–137 (1976).

34. Strohmeier, B. R. An ESCA method for determining the oxide thickness on aluminum alloys. *Surf. Interface Anal.* **15**, 51–56 (1990).

35. Tanuma, S., Powell, C. J. & Penn, D. R. Calculations of electron inelastic mean free paths for 31 materials. *Surf. Interface Anal.* **11**, 577–589 (1988).

36. Viroulaud, R. et al. Influence of surface pretreatments on the quality of trivalent chromium process coatings on aluminum alloy. *Appl. Surf. Sci.* **423**, 927–938 (2017).

37. Li, M., Wiame, F., Seyeux, A., Marcus, P. & Światowska, J. Effect of thermal oxidation on surface chemistry and elemental segregation of Al-Cu-Li alloy. *Appl. Surf. Sci.* **534**, 147633 (2020).

38. Ambat, R., Davenport, A. J., Scamans, G. M. & Afseth, A. Effect of iron-containing intermetallic particles on the corrosion behaviour of aluminium. *Corros. Sci.* **48**, 3455–3471 (2006).

39. Iannuzzi, M., Young, T. & Frankel, G. S. Aluminum alloy corrosion inhibition by vanadates. *J. Electrochem. Soc.* **153**, B533 (2006).

40. Iannuzzi, M. & Frankel, G. S. Mechanisms of corrosion inhibition of AA2024-T3 by vanadates. *Publ. Corros. Sci.* **49**, 2371–2391 (2007).

41. Natishan, P. M. Perspectives on chloride interactions with passive oxides and oxide film breakdown. *J. Sci. Eng.* **74**, 263–275 (2018).

42. Natishan, P. M. & O'Grady, W. E. Chloride ion interactions with oxide-covered aluminum leading to pitting corrosion: a review. *J. Electrochem. Soc.* **161**, 421–432 (2014).

43. Yasakau, K. A., Zheludkevich, M. L. & Ferreira, M. G. S. in *Intermetallic Matrix Composites* (ed. Mitra, R.) 425–462 (Woodhead Publishing, 2018).

44. Frankel, G. S. Pitting corrosion of metals: a review of the critical factors. *J. Electrochem. Soc.* **145**, 2186–2198 (1998).

45. Patterson, A. L. The Scherrer formula for X-ray particle size determination. *Phys. Rev.* **56**, 978–982 (1939).

46. Cullity, B. D. & Stock, S. R. *Elements of X-ray Diffraction* 3rd edn (Pearson Education Limited, 2014).

AUTHOR CONTRIBUTIONS
C.S.W. performed the experiments, including ball milling, SEM, XRD electrochemical tests, and data analysis, including TEM, XPS, and SIMS. J.C. conducted the XPS, SIMS, and TEM experiments and analyzed the resulting data. J.S. and W.G. helped in preliminary TEM data collection, R.K.G. conceptualized and supervised the whole study and received funding to perform the work. The manuscript was drafted by C.S.W., J.C., and R.K.G., and revised by all the authors.

COMPETING INTERESTS
The authors declare no competing interests.

ADDITIONAL INFORMATION
Supplementary information The online version contains supplementary material available at https://doi.org/10.1038/s41529-022-00225-5.

Correspondence and requests for materials should be addressed to R. K. Gupta.

Reprints and permission information is available at http://www.nature.com/reprints

Publisher's note Springer Nature remains neutral with regard to jurisdictional claims in published maps and institutional affiliations.